Seismic velocity variations at TCDP are controlled by MJO driven precipitation pattern and high fluid discharge properties

G. Hillers[a], M. Campillo[a], K.-F. Ma[b]

[a] *Institut des Sciences de la Terre, Université Joseph Fourier, CNRS, Grenoble, France*
[b] *Dpt. Earth Sciences, National Central University, Jhongli City, Taiwan*

Abstract

Using seismic noise based monitoring techniques we find that seismic velocity variations (dv/v) observed with the borehole array of the Taiwan Chelungpufault Drilling Project (TCDP) are controlled by strong precipitation events associated with the Madden-Julian Oscillation (MJO), a dynamic intraseasonal atmospheric pattern in the tropical atmosphere. High-frequency noise (>1 Hz) excited by steady anthropogenic activity in the vicinity of the TCDP allows daily resolution of dv/v time series. Relatively large fluid discharge properties control the equilibration of the ground water table and hence seismic velocities on time scales smaller than the average precipitation recurrence interval. This leads to the observed synchronous 50–80 day periodicity in dv/v and rainfall records in addition to the dominant annual component. Further evidence for the governing role of hydraulic properties is inferred from the similarity of observed dv/v timing, amplitude, and recovery properties with dv/v synthetics generated by a combined model of ground water table changes and diffusive propagation of seismic energy. The lapse time (τ) dependent increase of dv/v amplitudes is controlled by the sensitivity

of the diffuse wave field sampled at 1100 m depth to shallower water level fluctuations. The significant vertical offset between stations and water level explains the direct τ dependence which is opposite to the trend previously inferred from measurements at the surface.
Keywords: Ambient noise, Monitoring, Madden-Julian Oscillation, Borehole Seismology, Ground Water Table

1. Introduction

Interactions of atmospheric dynamics with solid Earth processes are manyfold (Tanimoto and Artru-Lambin, 2007). It includes triggering of slow earthquakes through low pressure systems (Liu et al., 2009), velocity changes in the upper crust by pressure fluctuations (Niu et al., 2008), and the excitation of seismic waves by nonlinear coupling of atmospheric disturbances with solid Earth through the ocean water column (Longuet-Higgins, 1950; Hasselmann, 1963). Reversely, ground motion excited by volcanic eruptions (Fee and Matoza, 2013) or earthquakes (Mutschlecner and Whitaker, 2005; Le Pichon et al., 2005) can propagate as pressure disturbances in the atmosphere. Through thermoelastic effects (Berger, 1975), temperature changes can cause seasonal variations in subsurface deformation (Prawirodirdjo et al., 2006) and in high-frequency noise excitation (Hillers and Ben-Zion, 2011). Precipitation triggers shallow seismicity and slope instabilities (Husen et al., 2007; Helmstetter and Garambois, 2010), and modulates regional seismic activity (Bettinelli et al., 2008) and seismic wave speeds (Meier et al., 2010) through variable water content in sedimentary basins.

In general these variations are characterized by an annual periodicity gov-

erned by the orbit of Earth and associated hemispheric weather pattern. Other repeat intervals of crustal processes in response to external forcing—i.e., neglecting phenomena governed by plate tectonics—are associated with tidal deformation, which are known to modulate volcanic and tectonic tremor activity (Custodio et al., 2003; Rubinstein et al., 2008), seismicity (Stroup et al., 2007), and subsurface wave speeds (Reasenberg and Aki, 1974).

In contrast to wave speed measurements based on intermittent explosive sources, methods based on the ubiquitous ambient seismic wave field constitute a powerful tool for continuous monitoring of seismic velocities (Campillo et al., 2011, and references therein). Noise based techniques are now routinely used to quantify fluctuations of crustal properties associated with volcanic activity (Brenguier et al., 2008b; Obermann et al., 2013a), earthquake deformation (Brenguier et al., 2008a; Rivet et al., 2011), water content and hydraulics (Sens-Schönfelder and Wegler, 2006; Meier et al., 2010; Froment et al., 2013), and tidal deformation (Hillers et al., 2013b). The temporal resolution of these methods is governed by the convergence rate of the noise correlation function, and is therefore frequency dependent (e.g., Larose et al., 2007); in the microseism frequency range resolution is usually on the order of days, but it can be improved using advanced data processing techniques (Baig et al., 2009; Hadziioannou et al., 2011).

Here we study seismic velocity changes (dv/v) using short period (>1 Hz) data recorded by the borehole array of the Taiwan Chelungpu-fault Drilling Project (TCDP, Fig. 1), which pierces the east dipping rupture plane of the 1999 M7.6 Chi-Chi thrust earthquake. The construction of daily high-SNR (signal-to-noise ratio) noise correlation functions benefits from steady noise

excitation through anthropogenic activity in the densely populated lowlands in western Taiwan (Hillers et al., 2012).

Knowledge of the system response to various loading mechanisms is essential for the assessment of potential earthquake triggering mechanisms in this active tectonic collision zone. Beyond the well documented seasonal periodicity we find that velocity variations are characterized by a significant intraseasonal 50–80 day spectral component. Analysis of meteorological data reveals that this pattern is controlled by strong precipitation events associated with the Madden-Julian Oscillation (MJO), a large-scale atmospheric circulation pattern in the tropic parts of the Indian and Pacific oceans (Zhang, 2005). We use the resulting dv/v time series to invert for hydraulic properties of the crust using a model of ground water level changes based on Darcy's law coupled to a diffusion model of scattered wave propagation (Sens-Schönfelder and Wegler, 2006, hereafter referred to as SSW06). Inversion results indicate that a relatively high drainage rate in the low-Q medium (Wang et al., 2010) hosting the Chi-Chi earthquake governs fast equilibration of the ground water table after strong precipitation events, which leads to the observed synchronous periodicity of dv/v and rainfall time series. We discuss that the experimental configuration, i.e., the vertical offset of the deep array from shallow water level variations, allows conclusions on the lapse time (τ) dependent sensitivity of the scattered wave field. The agreement between the observed τ dependence of dv/v amplitudes and the predicted τ dependence of depth-integrated sensitivity kernels verifies the accuracy of the diffusion model; the compatibility further indicates the possibility to constrain estimates of the scattering mean free path.

2. Velocity Variations

2.1. Data Processing

We process 3-component data from 6 TCDP short period (4.5 Hz) sensors installed between 946 m and 1274 m depth. For a detailed description of the recording environment and ambient wave field properties we refer the reader to Hillers et al. (2012). We compute daily correlation functions for all 9 components of the correlation tensor in two frequency (f) bands above 1 Hz for 2008 and 2009 using processing by Poli et al. (2012) to reduce the effects of transients. Different dv/v time series are created by constructing 'daily' correlations consisting of sub-stacks of d days ($\pm(d-1)/2$ days), where the choice of d affects SNR and temporal resolution. The best SNR is found for 1–4 Hz correlations (Hillers et al., 2012), which indicates sufficient sensitivity of the short period sensors below 4 Hz.

Noise based monitoring targets the lapse time (τ) dependent accumulation of arrival time changes ($d\tau$) of correlation coda phases associated with homogeneous relative velocity variations (dv/v) in a scattering medium, i.e., $dv/v = -d\tau/\tau$. Hillers et al. (2012) discussed that the obtained correlations are poor estimates of the inter-sensor Green's functions (GF). This is a result of the proximity of the TCDP to the noise excitation region, and the associated directionality of the incident wave field. Evidence for coda phase sensitivity to medium properties was demonstrated by re-correlation of the coda wave field, which leads to improved GF estimates.

Noise source dependent fluctuations in wave field properties can lead to spurious dv/v signals that are not associated with targeted changes in the propagation medium (Zhan et al., 2013). We therefore analyzed variations of

the spectral content, SNR, incidence angle, and rectilinearity (Hillers et al., 2012) for the two-year observation period. The stability of these auxiliary time series, and the sub-stack coherency with the reference stack (*cc*; Fig. 2a) discussed below, do not indicate a bias associated with excitation variations. We conclude that the correlation functions, though not fully converged GF, are sufficiently stable to facilitate wave speed monitoring (Hadziioannou et al., 2009).

For each of the 9 components, all correlations are stacked to create reference functions. We apply a time- and a frequency-domain technique ('stretching' and 'doublet' method) for daily estimates of dv/v. This allows a further assessment of the robustness of the results, because the methods perform different in the presence of pseudo-noise or wave field fluctuations (Hadziioannou et al., 2009, 2011). At each datum, the dv/v estimates obtained with the stretching method (Lobkis and Weaver, 2003) are averaged over the 15 inter-station times 9 inter-component results. Errors are estimated using the approach by Weaver et al. (2011) and scaled by the number of measurements (Hadziioannou et al., 2011). Weights associated with the two phase- and time-domain regressions constituting the doublet method (Poupinet et al., 1984; Clarke et al., 2011) allow a simultaneous inversion of all data, leading to results characterized by reduced daily fluctuations (estimated, e.g., during 01/2009) and error estimates. We perform the analysis for three sub-stack choices ($d = 1, 3, 7$ days) and three coda windows of 4 s duration defined by their average lapse time $\tau = 4, 8, 12$ s. We focus on the 1–4 Hz range because the noise intensity is proportional to $1/f$ (Hillers et al., 2012); at 2–8 Hz, dv/v amplitudes and the similarity of daily correlations to the reference stack

are significantly reduced.

2.2. Properties of Velocity Change Time Series

Overall, dv/v time series obtained with the two techniques are remarkably similar, yielding high confidence in the significance of the variations. The records are characterized by sudden velocity reductions during summer months in both years with peak amplitudes between 0.1–0.3%, which are followed by a recovery over days to tens of days to the background level. The lapse time τ controls peak dv/v estimates during velocity reduction episodes (Fig. 2b) and the overall coherency level. The τ dependence of the dv/v amplitude is robust considering the *cc* dependent (stretching) error estimates between 1.3×10^{-4} and 1.2×10^{-4} for $\tau = 4, 12$ s.

We analyze the spectral content of the dv/v time series in Figure 2 using two approaches. First, we apply a Lomb-Scargle (LS) algorithm to the incomplete time series (5% gaps; mostly associated with acquisition problems coincident with taifuns). Second, we interpolate the gaps and perform a standard DFT analysis. The results mutually support each other. Amplitude spectra are dominated by an annual signal (Fig. 3a); peaks with decreasing amplitude towards shorter periods are associated with overtones. However, peaks between 50–80 days (Fig. 3b) are not compatible with the decaying overtone pattern. The significance of this ridge is verified by estimating the spectra of a 'high-pass' time series, which is the residual between the original and a tens-of-day smoothed 'low-pass' time series.

A weak 7-day spectral component is the footprint of anthropogenic excitation (Hillers et al., 2012). Its τ dependent decrease indicates that randomization through scattering causes a progressive decay of characteristics inherited from

the source process (Paul et al., 2005).

2.3. Meteorological Data

Spectra of meteorological records (pressure P, temperature T, rainfall R; neglect of wind data) recorded 10 km west of the TCDP site (Fig. 1) are dominated by an annual periodicity (Fig. 3c). The rainfall spectrogram is characterized by a second significant peak of scaled amplitude 0.8 around 50–80 days (Fig. 3d), which resembles the dv/v pattern in Figure 3b. In comparison, corresponding P and T spectral amplitudes of $\sim$1/10 of the annual signal are significantly smaller.

The analysis shows that atmospheric dynamics in Taiwan are controlled by the Madden-Julian Oscillation (MJO), "the dominant component of the intraseasonal (30–90 days) variability in the tropical atmosphere" (Zhang, 2005). which is associated with a pattern of eastward propagating low pressure systems originating in the warm Indian and Pacific oceans. The MJO thus mostly affects precipitation rates, and the small intraseasonal P and T components correspond to pressure and temperature drops associated with rainfall events. Cross-correlation of hourly sampled high-pass P-R and T-R time series shows that pressure decreases $\sim$20–30 hours before rainfall, and temperature falls almost simultaneously with the onset of precipitation.

The coincidence of seismic velocity reductions with strong MJO driven precipitation events (Fig. 4), and the similarity of dv/v and R spectrograms imply that seismic wave speed changes are controlled by fluctuations of the water content in the upper crust. Similarly important for the emergence of the MJO spectral footprint in the dv/v data is the observed recovery on time scales smaller than the average large-precipitation periodicity.

3. Inversion for Hydraulic Parameters

3.1. The Model

We use the model of SSW06 (Sens-Schönfelder and Wegler, 2006) to validate the hypothesis of precipitation driven velocity changes and to estimate average hydraulic properties from the dv/v measurements. We briefly reproduce the four model building blocks which couple seismic velocity variations to precipitation rates and drainage properties; see Sens-Schönfelder and Wegler (2011) for a more detailed description.

(1) Darcy's law controls the exponential drainage of the water table through an aquifer after a rain event. Convolution of the precipitation rate p with this exponential decrease yields the ground water level GWL at time t_i measured in days,

$$GWL(t_i) = GWL_0 - \sum_{n=0}^{i} \phi^{-1} p(t_n) \exp\left[-(t_i - t_n)a\right], \qquad (1)$$

which depends on some unknown asymptotic level GWL_0, the porosity ϕ controlling the amplitude of the GWL variation in response to $p(t)$, and the decay parameter a; Helmstetter and Garambois (2010) use a similar formulation for the modeling of precipitation induced landslide triggering.

(2) The relative velocity perturbation $V(t_i, z)$ at depth z depends on the predicted $GWL(t_i)$, a reference water level GWL_{ref}, and δv, the relative velocity difference between drained and undrained states, i.e., $V(t_i, z) = \delta v$ for $GWL(t_i) < z < GWL_{\mathrm{ref}}$, $V(t_i, z) = -\delta v$ for $GWL_{\mathrm{ref}} < z < GWL(t_i)$, and $V(t_i, z) = 0$ elsewhere. The reference level is chosen to be the mean level over the period for the reference correlation stack for the dv/v analysis, i.e., the average over the two year analysis period.

(3) Energy propagation of the scattered coda wave field is modeled as a diffusion process (Pacheco and Snieder, 2005). Considering network dimensions and wavelength, we use a 3-D sensitivity kernel under the assumption of coincident source and receiver, $K_{3D}(\mathbf{x},\tau) = (2\pi Dr)^{-1}\exp[-r^2/(D\tau)]$. The distance between source/receiver and a point in space $\mathbf{x}$ is r, and D is the diffusion constant of seismic energy. Centered on the observation depth z_0 $K_{3D}(\mathbf{x},\tau)$ is integrated across the horizontal domain yielding $K(z,\tau)$. K is normalized by τ to ensure $\int K dz = 1$.

(4) The three components are combined to compute the delay time $d\tau$ at lapse time τ by integrating the velocity perturbation V weighted by the nonlinear kernel K:

$$d\tau_i(\tau) = d\tau(t_i,\tau) = \int_{z=0}^{\infty} \frac{K(z,\tau)}{V(t_i,z)} dz. \qquad (2)$$

The model allows an assessment of timing, amplitude, and recovery properties of the observed relative velocity variations by estimating GWL_0, ϕ, a, and δv. This is done by minimizing the residual P between the synthetic $(dv_i/v)_s = -d\tau_i/\tau$ (Eq. 2) and the observed $(dv_i/v)_o$ time series, $P = \sum_i \rho_i$, with $\rho_i = [(dv_i/v)_s - (dv_i/v)_o]^2$. Note the trade-off between ϕ and δv, i.e. $\delta s/\phi$ with $\delta s = \delta v^{-1}$. Small slowness perturbations associated with large GWL amplitudes (small ϕ) can not be resolved from large δs changes meeting small GWL fluctuations (large ϕ). Following SSW06 we use a genetic algorithm (GA) for the minimization of P. We analyze distributions of 150 independent estimates, because the rough fitness landscape is characterized by many local minima.

We consider two types of inversions. Separate lapse time dependent inversions are motivated by the observation that some drainage episodes show a

τ dependence of the decay behavior (e.g., 08/2008, 08/2009, Fig. 2b). In contrast, a joint inversion minimizes the residuals simultaneously for joint constraints of GWL_0, a, and $\delta s/\phi$.

3.2. Inversion Results

3.2.1. Timing

The similarity between $(dv_i/v)_\mathrm{o}$ and $(dv_i/v)_\mathrm{s}$ with respect to the timing of the dv/v drops (Fig. 4) supports the hypothesis of precipitation driven velocity variations. Performing separate inversions, we observe a τ dependent increase of the residual P, which is associated with the lapse time dependent increase in remnant coda fluctuations. This also causes larger P associated with $d = 1$ day dv/v time series for all τ compared to $d = 3$ and 7 days. Visual inspection of ρ_i time series reveals a d dependence of the misfit at large amplitude velocity drops. It implies that the disadvantage of small-d time series associated with small SNR is compensated by the better temporal resolution in response to rainfall, and indicates that the system response delay does not exceed one day. Yet better resolution can be obtained if fluctuations associated with diurnal excitation changes (Hillers et al., 2012) are mitigated (Baig et al., 2009; Hadziioannou et al., 2011). In the remainder of this work we use $d = 3$ days to balance the trade-off between temporal resolution and SNR.

3.2.2. Amplitude and Decay

The consistency between precipitation driven synthetic and observed dv/v levels indicates the applicability of the model for estimates of average hydraulic properties controlling GWL amplitude and decay. Amplitude refers

to the reduced dv/v value in response to rainfall (Fig. 4), and decay rates to the recovery speed controlled by drainage properties of the model aquifer. Amplitude estimates are sensitive to properties of $K(z,\tau)$ and therefore depend critically on the diffusion constant $D = lv/3$, which is proportional to wave velocity v and the scattering or elastic mean free path l. The mean free path describes the average distance between two scattering events and is consequently controlled by the medium heterogeneity (Aki and Richards, 1980). A direct estimate of l from spectral properties of $v(z)$ (Hillers et al., 2013a) is inhibited by the limited extension of the velocity log (Fig. 5a). However, the lower limit of D is constrained considering that l must be larger than the wavelength $\lambda = v/f$. We assume the 9-component average to be controlled by S-wave sensitivities ($v = v_S$), and that frequencies at the high-f edge of the 1–4 Hz range dominate the dv/v estimates (Hillers et al., 2012). With $f = 4$ Hz, $l/\lambda > 1$ for $D > 2-3\times10^5$ m^{2}s^{-1} (Fig. 5b), where we assume that l/λ tends to increase towards shallower depths. With an average v_S value this translates into $l > \lambda \approx 450$ m.

Using $D = 3 \times 10^5$ m^{2}s^{-1} in the separate inversions (Fig. 6), the a distributions confirm the visually inferred intermittent τ dependence in the dv/v time series. Lapse time independent GWL_0 distributions cluster around the peak-K level at z_0, so that the observed amplitudes are reproduced by the τ dependence of $\delta s/\phi$. This, however, implies different water levels fluctuations, which is not compatible with a single-aquifer model.

The depth range of the observed direct τ dependence is limited by the depth $z_\times$ at which the $K(z,\tau)$-functions intersect (Figs. 5c–e). This behavior is utilized in a joint inversion (Fig. 7), where the three τ dependent measure-

ments constrain the asymptotic water level to $0 < z < z_\times$ and resolve the GWL_0-$\delta s/\phi$ trade-off. Consequently, the average depth of a resulting GWL_0 distribution is compatible with the associated D dependent $z_\times$ estimate.

Larger diffusion constants flatten the kernels and cause a reduction of (peak) K values. The GWL_0 sensitivity of $\delta s/\phi$ thus follows from the constraint of a constant $d\tau$ amplitude (Eq. 2). The role of ϕ as a tuning parameter becomes evident if we assume that δs is independent of depth. It explains why associated ϕ estimates are smaller compared to porosity measurements from TCDP rock samples (Wang et al., 2009).

It should be noted that the TCDP dv/v variations are an order of magnitude smaller compared to the ∼2% reported by SSW06. We attribute this to the shorter distance between stations at the surface and the inferred GWL level above 40 m at Mt. Merapi. Water table changes occur near the K-peak, and this effect is amplified by the smaller diffusion constant $D = 5 \times 10^4$ m^{2}s^{-1} (note that K values in Fig. 7 in Sens-Schönfelder and Wegler (2011) are erroneous).

Properties governing the drainage rate (0.02–0.03 d^{-1}) are independent of these amplitude controlling factors. The 2–3 times larger estimate compared to the experiment at Mt. Merapi (0.008 d^{-1}) indicates that the crust hosting the Chi-Chi earthquake is characterized by a more efficient fluid percolation network.

4. Discussion and Conclusions

Our high-frequency noise based monitoring analysis shows that seismic velocity variations (dv/v) measured with a borehole array of the Taiwan

Chelungpu-fault Drilling Project (TCDP) are characterized by a significant intraseasonal periodicity in addition to the annual spectral component frequently observed in dv/v studies (Meier et al., 2010; Froment et al., 2013). We find that the 50–80 day period matches properties of the precipitation pattern in Taiwan which is driven by the dynamics of the Madden-Julian Oscillation (MJO). Further evidence for the governing role of hydraulic properties is inferred from the similarity of averaged dv/v timing, amplitude, and recovery properties with dv/v synthetics. The adopted model synthesizes dv/v changes based on ground water level (GWL) fluctuations controlled by precipitation data and Darcy's law coupled to the sensitivity K of the scattered seismic wave field (Sens-Schönfelder and Wegler, 2006, abr. "SSW06"). The plausibility of this model is demonstrated by the remarkable consistency between multiple model components and observations in response to K-controlling variations of the diffusion constant D. Estimates of hydraulic parameters that govern the velocity response function to precipitation indicate a relatively large fluid mobility compared to estimates from a usually highly fractured volcanic environment (SSW06). High drainage properties facilitate the GWL equilibration on time scales shorter than the average precipitation interval, and thus constitute a necessary condition for the dv/v pattern to follow the MJO rhythm. Efficient drainage properties are compatible with observations of low Q values (Wang et al., 2010), which are likely associated with widespread damage induced by the 1999 M7.6 Chi-Chi earthquake.

Residual time series ρ_i indicate the difficulty to match amplitude and recovery properties associated with individual precipitation events using average

estimates of the model parameters (Fig. 4a). The intermittently observed lapse time dependence of a implies spatially variable hydraulic conditions and is thus incompatible with the assumption of a laterally homogeneous 1-D aquifer. Resolution of such second-order inconsistencies requires deciphering the complex hydraulic situation associated with subsurface fluid percolation properties and the spatio-temporal variation of precipitation. While the utilized rainfall time series $p(t)$ is characterized by high temporal resolution, it constitutes only a proxy of the actual rainfall pattern over the area that controls dv/v estimates (Bell, 1987). Figure 1 illustrates estimates of precipitation distributions observed from space. The large variability is indicated by the 60% contours of cumulative rainfall during days defined by the 10 largest daily amounts of precipitation recorded at the meteorologic station. The contours indicate that maximum precipitation occurs mostly in areas that do not include the rain gauge. The crustal structure in the tectonic collision zone is characterized by a dipping geology. Together with strong Q discontinuities across the Chelungpu fault (Wang et al., 2012), the implied variable drainage properties further contribute to the difficulties in reproducing the observed dv/v time series using average model parameters. It also challenges the assumption of isotropic propagation of the scattered wave field, which underpins the construction of K.

The range of 0.1–0.3% velocity reduction in response to significant precipitation is comparable to or somewhat larger than peak values reported for dv/v in response to rainfall (0.1%, Meier et al., 2010) and deformation due to earthquakes (0.5%,<0.1%, 0.2%, Wegler and Sens-Schönfelder, 2007; Brenguier et al., 2008a; Froment et al., 2013), volcanic activity (<0.1%, Brenguier

et al., 2008b), and slow slip events (0.2%, Rivet et al., 2011). However, our estimates are an order of magnitude smaller than the 2% variations at Mt. Merapi (SSW06). We attribute this to different K sensitivities associated with variable diffusion constants and different distances between the observation depth z_0 and the level of GWL changes. In addition to the direct poroelastic effect where the presence of water slows seismic wave propagation (Grêt et al., 2006), a loading effect can alter wave speeds. Similar to atmospheric pressure changes (Silver et al., 2007; Niu et al., 2008), water table fluctuations induce variable loads on the rock matrix below GWL—or at least below some impermeable layer such as the ∼300 m thick dipping formation that hosts the Chelungpu fault. However, this direct effect causes a dv/v fluctuation of opposite sign in the far field of an observation borehole. It may therefore contribute to the observed dv/v values by counterbalancing the poroelastic effect, but it does not dominate the wave speed variations. We do not find evidence that atmospheric pressure or temperature changes bias the discussed first order properties of the dv/v time series associated with timing, amplitude, and decay properties, either through surface loading effects or through perturbations of the conditions in the borehole.

The precipitation driven dv/v inverse amplitude dependence (smaller negative values) on lapse time reported by SSW06 is opposite to our observation showing a direct τ dependence (larger negative values; Fig. 2b). The effect is controlled by the relative position of z_0 and the water table change with respect to the intersection level $z_\times$ of the kernels $K(z,\tau)$ (Figs. 5c–e). In addition to constraining the equilibrium level GWL_0, this behavior allows estimates of the scattering mean free path $l = 3D/v_S$. The lower limit is

imposed by the wavelength, $l > \lambda \approx 450$ m, and the direct τ dependence of the dv/v amplitudes constrains together with the inverse τ dependence for all $z < z_0$ for $D > 5 \times 10^5$ m^{2}s^{-1} (Fig. 5e) the upper limit to $l < 850$ m. Estimates of l are likely to decrease towards shallower depth considering the velocity gradient above 600 m and the mountain topography. However, depth variable scattering properties are not considered in the 3-D isotropic wave propagation model underlying the analytic expression of $K(\mathbf{x}, \tau)$.

SSW06 conclude that the coda wave field at Mt. Merapi consists of body waves instead of surface waves. For primary sources located at the surface, the dominance of body waves implies a short mean free time (Obermann et al., 2013b), which is compatible with the small diffusion constant. TCDP noise at 1100 m depth is similarly dominated by body waves (Hillers et al., 2012), indicating that our analysis is not biased by the neglected conversions between surface and body waves.

Application of the 1-D joint inversion to situations in which the data quality is inferior, or where the signal is weaker, can benefit from a range of potential improvements. These include but are not limited to the denoising of noise correlation coda (Stehly et al., 2008; Baig et al., 2009); the construction of spatially averaged rainfall time series; the construction of kernels considering wave conversions; the application of kernels based on radiative transfer theory (Planes et al., 2014, and references therein), which have different sensitivities at early lapse times and short distances compared to the diffusion approximation (Obermann et al., 2013b); and the application of weighted misfit functions ρ_i. With these optimizations, the approach has the potential to constrain water level changes associated with anthropogenic activity such

as impoundment, ground water depletion, or the injection and extraction of fluids in the context of reservoir engineering.

Precipitation can trigger seismicity (Husen et al., 2007; Bettinelli et al., 2008; Helmstetter and Garambois, 2010; Hainzl et al., 2013). From an earthquake source physics point of view it is interesting to isolate the mechanism that controls variations in the nucleation rate, e.g., fault lubrication or pressurization, or changes in the loading rate caused by underground accumulation of water. We analyzed a regional earthquake catalog for correlations between daily rainfall and seismic event rates (Helmstetter and Garambois, 2010) using a systematic grid search over variable spatial and magnitude bins. The method detects a few coincidences, but the lack of systematic triggering in the associated space and magnitude intervals does not indicate a relevant physical mechanism.

We conclude by iterating the beneficial role steady anthropogenic activity plays in the construction of daily high-frequency correlation functions. Considering the additional information contained in decorrelation time series (Larose et al., 2010; Obermann et al., 2013a) we emphasize the relative stability of coherency measurements compared to dv/v fluctuations (Fig. 2a). It implies that the scattering properties do not change. This can be different for extended network geometries that contain areas impacted by strong rainfall events. In such a situation, analyses of dv/v and decorrelation data can target the interaction of the ambient wave field with evolving hydraulic situations.

Acknowledgments This work was supported by the European Research

414 Council (Advanced grant Whisper L27507). GH acknowledges support through
415 a Heisenberg fellowship from the German Research Foundation. Figures were
416 made using GMT (Wessel and Smith, 1991). Data used in this study were
417 produced with the Giovanni online data system, developed and maintained
418 by the NASA GES DISC. We acknowledge the helpful comments of C. Sens-
419 Schönfelder and an anonymous reviewer.

420 Aki, K., Richards, P. G. (Eds.), 1980. Quantitative Seismology, 1st Edition.
421 W. H. Freeman and Company, San Francisco.

422 Baig, A. M., Campillo, M., Brenguier, F., 2009. Denoising seismic noise
423 correlations. J. Geophy. Res. 114.

424 Bell, T. L., 1987. A Space-Time Stochastic Model of Rainfall for Satellite
425 Remote-Sensing Studies. J. Geophy. Res. 92 (D8), 9631–9643.

426 Berger, J., 1975. A Note on Thermoelastic Strains and Tilts. J. Geophy. Res.
427 80 (2), 274–277.

428 Bettinelli, P., Avouac, J.-P., Flouzat, M., Bollinger, L., Ramillien, G., Ra-
429 jaure, S., Sapkota, S., 2008. Seasonal variations of seismicity and geodetic
430 strain in the Himalaya induced by surface hydrology. Earth and Planetary
431 Science Letters 266, 332–344.

432 Brenguier, F., Campillo, M., Hadziioannou, C., Shapiro, N. M., Nadeau,
433 R. M., Larose, E., 2008a. Postseismic Relaxation Along the San Andreas
434 Fault at Parkfield from Continuous Seismological Observations. Science
435 321.

436 Brenguier, F., Shapiro, N. M., Campillo, M., Ferrazzini, V., Duputel, Z.,
437 Coutant, O., Nercessian, A., 2008b. Towards forecasting volcanic eruptions
438 using seismic noise. Nature Geoscience 1, 126–130.

439 Campillo, M., Sato, H., Shapiro, N. M., van der Hilst, R. D., 2011. New devel-
440 opments on imaging and monitoring with seismic noise. C. R. Geoscience
441 343, 487–495.

442 Clarke, D., Zaccarelli, L., Shapiro, N. M., Brenguier, F., 2011. Assessment of
443 resolution and accuracy of the Moving Window Cross Spectral technique
444 for monitoring crustal temporal variations using ambient seismic noise.
445 Geophys. J. Int. 186, 867–882.

446 Custodio, S. I. S., Fonseca, J. F. B. D., d'Oreye, N. F., Faria, B. V. E.,
447 Bandomo, Z., 2003. Tidal modulation of seismic noise and volcanic tremor.
448 Geophys. Res. Lett. 30 (15).

449 Fee, D., Matoza, R. S., 2013. An overview of volcano infrasound: From
450 hawaiian to plinian, local to global. J. Volcanol. Geotherm. Res. 249, 123–
451 139.

452 Froment, B., Campillo, M., Chen, J. H., Liu, Q. Y., 2013. Deformation at
453 depth associated with the 12 May 2008 MW 7.9 Wenchuan earthquake
454 from seismic ambient noise monitoring. Geophys. Res. Lett. 40, 78–82.

455 Grêt, A., Snieder, R., Scales, J., 2006. Time-lapse monitoring of rock prop-
456 erties with coda wave interferometry. J. Geophy. Res. 111.

457 Hadziioannou, C., Larose, E., Baig, A., Roux, P., Campillo, M., 2011. Im-
458 proving temporal resolution in ambient noise monitoring of seismic wave
459 speed. J. Geophy. Res. 116.

460 Hadziioannou, C., Larose, E., Coutant, O., Roux, P., Campillo, M., 2009.
461 Stability of monitoring weak changes in multiply scattering media with
462 ambient noise correlations: Laboratory experiments. J. Acoust. Soc. Am.
463 125 (6), 3688–3695.

464 Hainzl, S., Ben-Zion, Y., Cattania, C., Wassermann, J., 2013. Testing atmo-
465 spheric and tidal earthquake triggering at Mt. Hochstaufen, Germany. J.
466 Geophy. Res.

467 Hasselmann, K., 1963. A Statistical Analysis of the Generation of Micro-
468 seisms. Rev. Geophys. 1 (2), 177–210.

469 Helmstetter, A., Garambois, S., 2010. Seismic monitoring of Séchilienne rock-
470 slide (French Alps): Analysis of seismic signals and their correlation with
471 rainfalls. J. Geophy. Res. 115.

472 Hillers, G., Ben-Zion, Y., 2011. Seasonal variations of observed noise ampli-
473 tudes at 2–18 Hz in southern California. Geophys. J. Int. (184), 860–868.

474 Hillers, G., Ben-Zion, Y., Landès, M., Campillo, M., 2013a. Interaction of
475 microseisms with crustal heterogeneity: A case study from the San Jacinto
476 fault zone area. Geochem. Geophys. Geosyst. 14 (7).

477 Hillers, G., Campillo, M., Lin, Y.-Y., Ma, K.-F., Roux, P., 2012. Anatomy
478 of the high-frequency ambient seismic wave field at the TCDP borehole.
479 J. Geophy. Res. 117.

Hillers, G., Retailleau, L., Campillo, M., Inbal, A., Rivera, L., Ma, K.-F., Ampuero, J.-P., Nishimura, T., 2013b. Noise-based observation of wave speed variations associated with tidal loading: In-situ acoustoelastic testingSSA Abstract 13-165.

Husen, S., Bachmann, C., Giardini, D., 2007. Locally triggered seismicity in the central Swiss Alps following the large rainfall event of August 2005. Geophys. J. Int. 171, 11261134.

Larose, E., Planes, T., Rossetto, V., Margerin, L., 2010. Locating a small change in a multiple scattering environment. Appl. Phys. Lett. 96.

Larose, E., Roux, P., Campillo, M., 2007. Reconstruction of Rayleigh-Lamb dispersion spectrum based on noise obtained from an air-jet forcing. J. Acoust. Soc. Am. 122 (6), 3437–3444.

Le Pichon, A., Herry, P., Mialle, P., Vergoz, J., Brachet, N., Garcés, M., Drob, D., Ceranna, L., 2005. Infrasound associated with 2004–2005 large Sumatra earthquakes and tsunami. Geophys. Res. Lett. 32.

Liu, C., Linde, A. T., Sacks, I. S., 2009. Slow earthquakes triggered by typhoons. Nature 459, 833–836.

Lobkis, O. I., Weaver, R. L., 2003. Coda-Wave Interferometry in Finite Solids: Recovery of p-to-s Conversion Rates in an Elastodynamic Billiard. Phys. Rev. Lett. 90 (25).

Longuet-Higgins, M. S., 1950. A theory of the origin of microseisms. Phil. Trans. R. Soc. London, Ser. A 243, 1–35.

Meier, U., Shapiro, N. M., Brenguier, F., 2010. Detecting seasonal variations in seismic velocities within Los Angeles basin from correlations of ambient seismic noise. Geophys. J. Int. 181, 985–996.

Mutschlecner, J. P., Whitaker, R. W., 2005. Infrasound from earthquakes. J. Geophy. Res. 110.

Niu, F., Silver, P. G., Daley, T. M., Cheng, X., Majer, E. L., 2008. Preseismic velocity changes observed from active source monitoring at the parkfield SAFOD drill site. Nature 454, 204–208.

Obermann, A., Planès, T., Larose, E., Campillo, M., 2013a. Imaging preeruptive and coeruptive structural and mechanical changes of a volcano with ambient seismic noise. J. Geophy. Res. 118, 6285–6294.

Obermann, A., Planès, T., Larose, E., Sens-Schönfelder, C., Campillo, M., 2013b. Depth sensitivity of seismic coda waves to velocity perturbations in an elastic heterogeneous medium. Geophys. J. Int. 194 (1), 372–382.

Pacheco, C., Snieder, R., 2005. Time-lapse travel time change of multiply scattered acoustic waves. J. Acoust. Soc. Am. 118 (3), 1300–1310.

Paul, A., Campillo, M., Margerin, L., Larose, E., Derode, A., 2005. Empirical synthesis of time-asymmetrical Green function from the correlation of coda waves. J. Geophy. Res. 110.

Planes, T., Larose, E., Margerin, L., Rossetto, V., Sens-Schönfelder, C., 2014. Decorrelation and phase-shift of coda waves induced by local changes: multiple scattering approach and numerical validation. Waves in Random and Complex MediaIn press.

525 Poli, P., Pedersen, H. A., Campillo, M., the POLENET/LAPNET Work-
526 ing Group, 2012. Emergence of body waves from cross-correlation of short
527 period seismic noise. Geophys. J. Int. 188, 549–558.

528 Poupinet, G., Ellsworth, W., Frechet, J., 1984. Monitoring Velocity Vari-
529 ations in the Crust Using Earthquake Doublets: An Application to the
530 Calaveras Fault, California. J. Geophy. Res. 89 (B7), 5719–5731.

531 Prawirodirdjo, L., Ben-Zion, Y., Bock, Y., 2006. Observation and Modeling
532 of Thermoelastic Strain in SCIGN Daily Position Time Series. J. Geophy.
533 Res. 111.

534 Reasenberg, P., Aki, K., 1974. A Precise, Continuous Measurement of Seismic
535 Velocity for Monitoring In Situ Stress. J. Geophy. Res. 79 (2), 399–406.

536 Rivet, D., Campillo, M., Shapiro, N. M., Cruz-Atienza, V., Radiguet, M.,
537 Cotte, N., Kostoglodov, V., 2011. Seismic evidence of nonlinear crustal
538 deformation during a large slow slip event in Mexico. Geophys. Res. Lett.
539 38.

540 Rubinstein, J. L., Rocca, M. L., Vidale, J. E., Creager, K. C., Wech, A. G.,
541 2008. Tidal Modulation of Nonvolcanic Tremor. Science 319, 186–189.

542 Sens-Schönfelder, C., Wegler, U., 2006. Passive image interferometry and
543 seasonal variations of seismic velocities at Merapi Volcano, Indonesia. Geo-
544 phys. Res. Lett. 33.

545 Sens-Schönfelder, C., Wegler, U., 2011. Passive image interferometry for mon-
546 itoring crustal changes with ambient seismic noise. C. R. Geoscience 343,
547 639–651.

548 Silver, P. G., Daley, T. M., Niu, F., Majer, E. L., 2007. Active Source Moni-
549 toring of Cross-Well Seismic Travel Time for Stress-Induced Changes. Bull.
550 Seism. Soc. Am. 97 (1B), 281–293.

551 Stehly, L., Campillo, M., Froment, B., Weaver, R. L., 2008. Reconstruct-
552 ing Green's function by correlation of the coda of the correlation (c^3) of
553 ambient seismic noise. J. Geophy. Res. 113 (B11306).

554 Stroup, D. F., Bohnenstiehl, D. R., Tolstoy, M., Waldhauser, F., Weekly,
555 R. T., 2007. Pulse of the seafloor: Tidal triggering of microearthquakes at
556 9°50′N East Pacific Rise. Geophys. Res. Lett. 34.

557 Tanimoto, T., Artru-Lambin, J., 2007. Interaction of Solid Earth, Atmo-
558 sphere and Ionosphere. In: Schubert, G. (Ed.), Treatise on Geophysics.
559 Vol. 4. Elsevier, Oxford, U.K., pp. 421–444.

560 Wang, J.-H., Hung, J.-H., Dong, J.-J., 2009. Seismic velocities, density,
561 porosity, and permeability measured at a deep hole penetrating the
562 Chelungpu fault in central Taiwan. J. Asian Earth Sci. 36, 135–145.

563 Wang, Y.-J., Lin, Y.-Y., Ma, K.-F., Lee, M.-C., 2012. Fault Zone Q structure
564 discovered from the Taiwan Chelungpu Fault Borehole Seismometer array
565 (TCDPBHS). Tectonophysics 578, 76–86.

566 Wang, Y.-J., Ma, K.-F., Mouthereau, F., Eberhart-Phillips, D., 2010. Three-
567 dimensional Qp- and Qs-tomography beneath Taiwan orogenic belt: impli-
568 cations for tectonic and thermal structure. Geophys. J. Int. 180, 891–910.

569 Weaver, R. L., Hadziioannou, C., Larose, E., Campillo, M., 2011. On the

precision of noise correlation interferometry. Geophys. J. Int. 185, 1384–1392.

Wegler, U., Sens-Schönfelder, C., 2007. Fault zone monitoring with passive image interferometry. Geophys. J. Int. 168, 1029–1033.

Wessel, P., Smith, W. H. F., 1991. Free software helps map and display data. Eos Trans. AGU 72.

Wu, H.-Y., Ma, K.-F., Zoback, M., Boness, N., Ito, H., Hung, J.-H., Hickman, S., 2007. Stress orientation of Taiwan Chelungpu-Fault Drilling Project (TCDP) hole-A as observed from geophysical logs. Geophys. Res. Lett. 34.

Zhan, Z., Tsai, V. C., Clayton, R. W., 2013. Spurious velocity changes caused by temporal variations in ambient noise frequency content. Geophys. J. Int.

Zhang, C., 2005. Madden-Julian Oscillation. Rev. Geophys. 43.

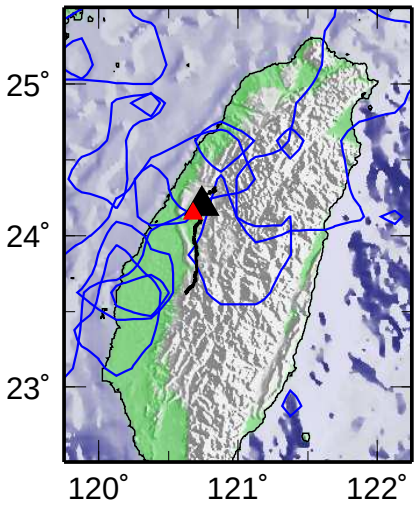

Figure 1: The map of the study area indicates locations of the TCDP site (black triangle) and the meteorologic station (red triangle). Anthropogenic seismic noise is excited in the green indicated lowland southwest of the TCDP (Hillers et al., 2012). The black line beneath the TCDP is the surface trace of the east dipping Chelungpu fault. Blue lines indicate precipitation distributions observed from space. Each line represents the 60% contour of cumulative rainfall during the 10 days in 2008 and 2009 defined by peak precipitation events.

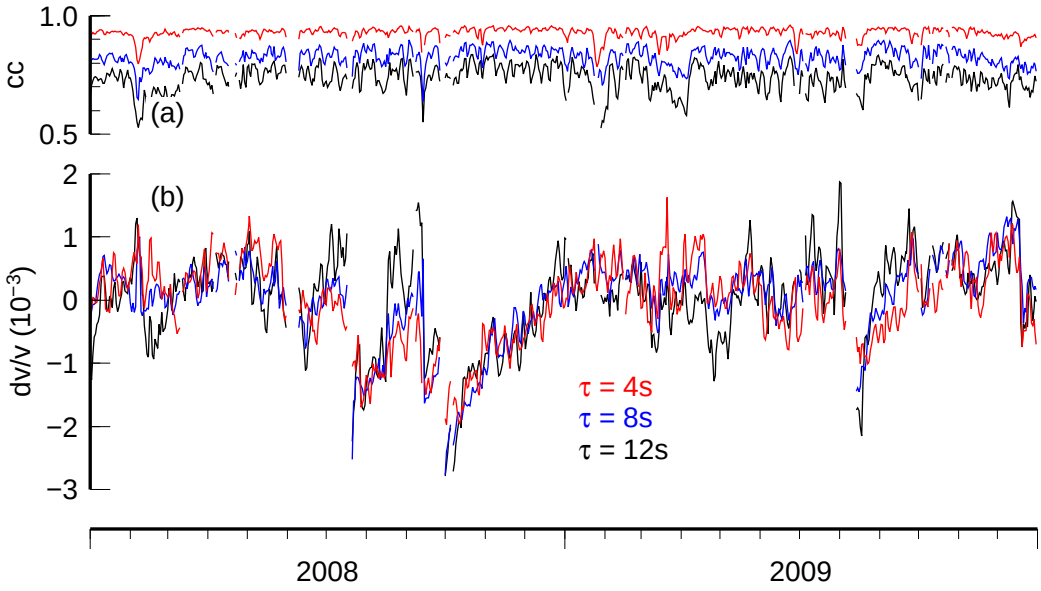

Figure 2: (a) Coherency estimates associated with (b) relative velocity changes (dv/v) measured with the stretching technique using three different coda lapse time windows. The frequency range is 1–4 Hz, and $d = 3$.

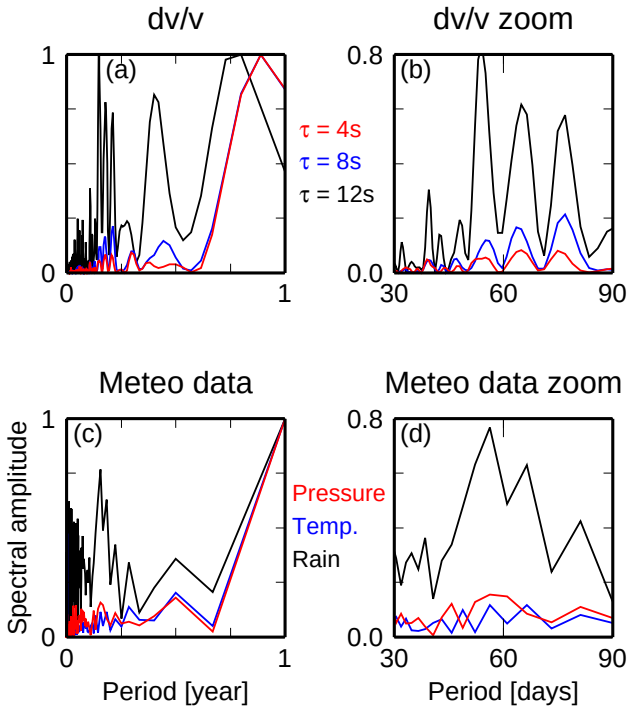

Figure 3: (a) Spectral amplitudes of lapse time (τ) dependent dv/v observations. Colors as in Figure 2. Amplitudes are scaled to the annual component. (b) Zoom on the MJO pattern. (c) Spectral amplitudes of rainfall, temperature, and atmospheric pressure records. Amplitudes are scaled to the annual component. (d) Zoom on the MJO pattern.

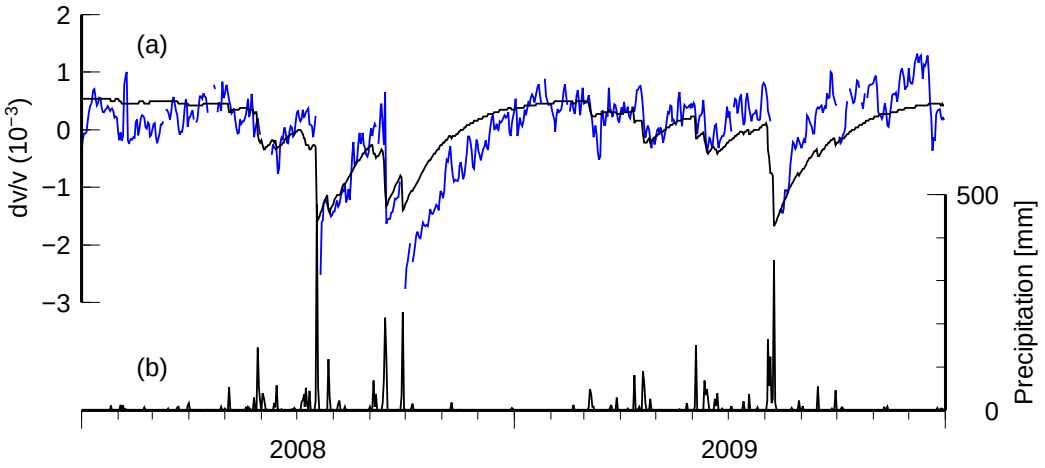

Figure 4: (a) Blue: Observed dv/v time series ($\tau = 8$ s). Black: Synthetic dv/v estimates based on the model described in Section 3. The consistency indicates that the model can explain first order characteristics of the measurements associated with timing, amplitude, and drainage. Resolution of the dv/v synthetics (vertical discretization of the black curve) is controlled by the vertical resolution dz of the kernel K. (b) The model ground water level (Eq. 1) is driven by daily precipitation records collected 8 km southwest of the TCDP site (Fig. 1).

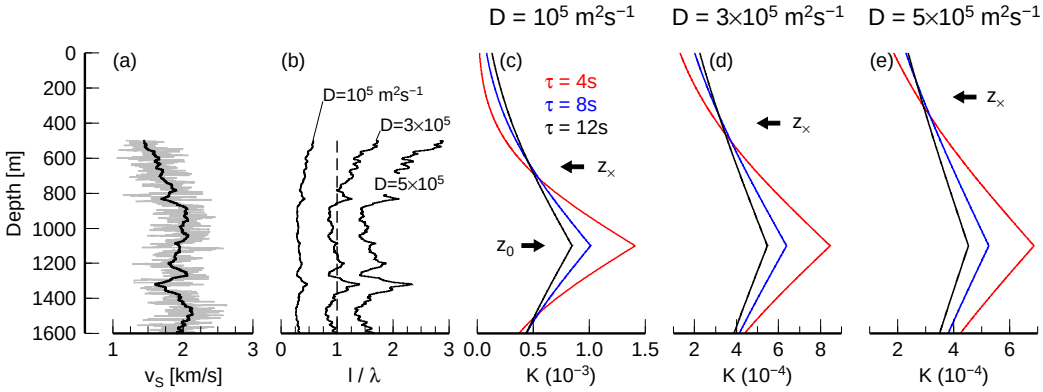

Figure 5: (a) Section of the shear wave velocity log (gray; data are available between 500 m and 1850 m; Wu et al., 2007) and its 50 m average (black). (b) The ratio of scattering mean free path ($l = 3D/v_S$) and wavelength ($\lambda = v_S/f$) using an average v_S profile, $f = 4$ Hz, and a range of diffusion constants D. It should be noted that D cannot be defined on scales indicated by the vertical l/λ resolution. However, the distributions illustrate the range of plausible D values for which $l > \lambda$. (c)–(e): D dependent distributions of the kernel $K(z, \tau)$ associated with the observation depth $z_0 = 1100$ m. The τ dependence of velocity change amplitudes is controlled by the water level relative to the intersection depth $z_\times$.

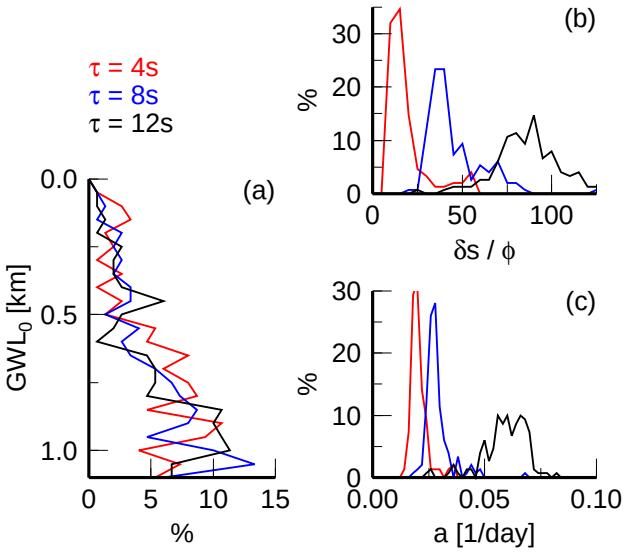

Figure 6: Distributions of the hydraulic parameters (Eq. 1) obtained from 150 separate inversions using $D = 3 \times 10^5$ m^{2}s^{-1}. Colors indicate lapse time. (a) Equilibrium ground water table GWL_0 (bin width 50 m). The search range is limited to $z < z_0$. (b) Slowness sensitivity $\delta s/\phi$ (bin width 5). (c) Decay rate a (bin width 0.002 1/day). The residual R is uniformly distributed across the parameter space.

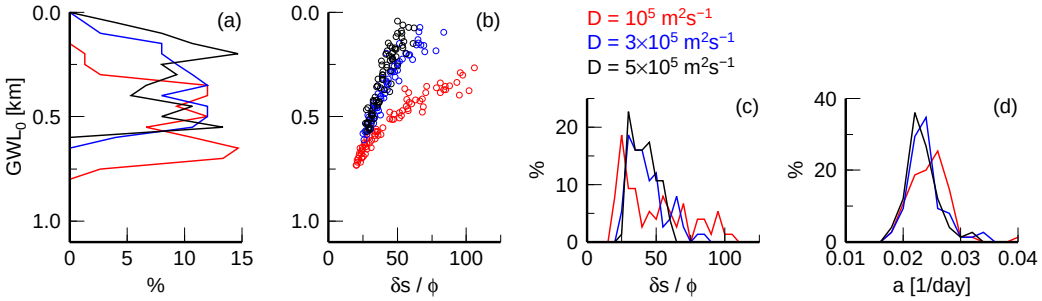

Figure 7: Distributions of the hydraulic parameters (Eq. 1) associated with 150 joint inversions. We show the best 50% because the residual R is sensitive to GLW_0. Colors indicate the diffusion constant which controls the depth sensitivity of the kernel K. We used a range of D values to illustrate the sensitivity of the solutions to the crossing depth $z_\times$ (Figs. 5c–e), although $D < 2 \times 10^5$ m^{2}s^{-1} might be unphysical (Fig. 5b). (a) Equilibrium ground water table GWL_0 (bin width 50 m). (b) Dependence of $\delta s/\phi$ on GWL_0. (c) Slowness sensitivity $\delta s/\phi$ (bin width 5). (d) Decay rate a (bin width 0.002 1/day). There is no dependence of a on GWL_0.